High-Density Litz-Wired Integrated Magnetics Combining OBC and LDC Transformers With an Integrated Resonant Inductor for Electric Vehicle Charging Systems

Chenli Zhou, Jianping Xu, Jinzhu Xu, Jun Liu, and Rui Huang

***Abstract*—Integrated on-board charger (OBC) and low-voltage dc–dc converter (LDC) system is attractive for electric vehicles due to its reduced number of switching devices and magnetic components. This article proposes a novel high-density integrated magnetic component (IMC) that achieves the integration of the high-frequency transformers of the OBC and the LDC with the resonant inductor of the OBC, which reduces the cost, the weight, and the volume of the charging system. Based on the proposed IMC, the system can simultaneously charge the high-voltage battery (HVB) and the low-voltage battery (LVB). Moreover, an elliptical ring-shaped magnetic shunt is employed to achieve controllable leakage inductance, and Litz wire is adopted to replace the conventional busbar winding of the LDC to reduce eddy-current losses and support high-current output. Detailed analysis and design guideline of the proposed IMC are provided. To validate the feasibility of the proposed IMC, a prototype with an integrated 6.6 kW OBC and 2 kW LDC is built. The experimental results show that the proposed IMC achieves a power density of 660 W/in^3 and enables the prototype to achieve a peak efficiency of 98.17% at full load during OBC operation.**

***Index Terms*—Electric vehicles (EVs), Litz wire, low-voltage dc–dc converter (LDC), magnetic integration, on-board charger (OBC), resonant converter.**

NOMENCLATURE

Abbreviations

LDC	Low-voltage dc–dc converter.
IMC	Integrated magnetic component.
VCS	Vehicle charging system.
HVB	High-voltage battery.
LVB	Low-voltage battery.
BDR	Buck-derived rectifier.
SPS	Single-phase shift.
TPS	Triple-phase-shift.
TPSRC	Three-port series resonant converter.
VDR	Voltage doubler rectifier.
PSFB	Phase shift full bridge.
CTR	Center-tap rectifier.

Symbols

$N_\mathrm{p}, N_\mathrm{s}, N_\mathrm{t}$	Number of turns of the primary, secondary, and tertiary windings.
$L_\mathrm{p}, L_\mathrm{s}, L_\mathrm{t}$	Leakage inductance of the primary, secondary, and tertiary windings.
V_bus	Bus voltage.
V_HV	Output voltage of the OBC.
V_LV	Output voltage of the LDC.
I_Pmax	Peak current of the primary winding.
n	Transformer's turns ratio.
k	Voltage conversion ratio of the OBC.
N_0	Number of strands.
$X_\mathrm{r,pu}$	Per-unit resonant reactance.
F_1, F_2, F_3	Magnetomotive forces.
E_air	Leakage-field energy stored in the air.
l_mean	Effective field path length.
r	Chamfer radius of the center leg.
l_s	Thickness of the magnetic shunt.
C_1, C_2	Half of the circumference of the magnetic shunt.
δ_1, δ_2	Air gap.
k, α, β	Constants determined by magnetic material.
R_shunt	Reluctance of the magnetic shunt.
$R_\mathrm{g1}, R_\mathrm{g2}$	Air-gap reluctance.
$D_\mathrm{p}, D_\mathrm{s}$	Internal phase shift duty cycle of the SRC.
D_ϕ, D_f	Phase shift duty cycle of the SRC.

I. INTRODUCTION

ELECTRIC vehicles (EVs) have attracted much attention in industry and academia due to their environmentally

Received 30 July 2025; revised 14 October 2025 and 24 November 2025; accepted 7 January 2026. Date of publication 12 January 2026; date of current version 20 March 2026. This work was supported by the National Natural Science Foundation of China under Grant 52477198 and Grant 52407224. Recommended for publication by Associate Editor S. Lee. *(Corresponding author: Jianping Xu.)*

Chenli Zhou, Jianping Xu, and Rui Huang are with the School of Electrical Engineering, Southwest Jiaotong University, Chengdu 611756, China, and also with the Key Laboratory of Magnetic Suspension Technology and Maglev Vehicle, Ministry of Education, Chengdu 611756, China (e-mail: zhouchenli@my.swjtu.edu.cn; jpxu@swjtu.edu.cn; ruihuang@my.swjtu.edu.cn).

Jinzhu Xu and Jun Liu are with Shenzhen VMAX New Energy (Group) Company Ltd., Shenzhen 518000, China (e-mail: xujinzhu@vmaxpower.com.cn; jefferson@vmaxpower.com.cn).

Color versions of one or more figures in this article are available at https://doi.org/10.1109/TPEL.2026.3652738.

Digital Object Identifier 10.1109/TPEL.2026.3652738

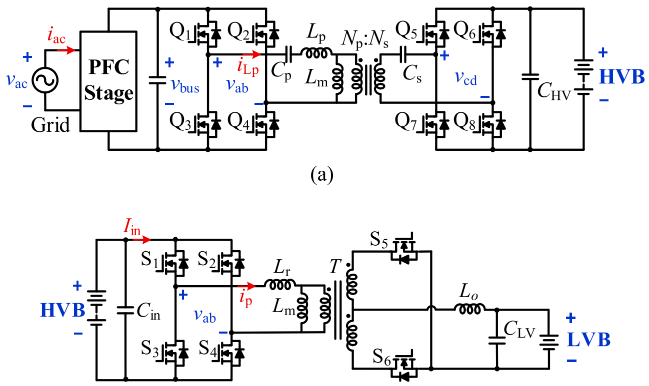

Fig. 1. Circuit topology of the conventional VCS. (a) OBC. (b) LDC.

benefits and high energy efficiency [1], [2]. VCS, which consists of an OBC and an LDC, serves as a key subsystem of the electric powertrain of EVs. In the VCS, OBC is designed to charge the HVB, and LDC supplies power to various low-voltage auxiliary loads.

In the conventional VCS, as shown in Fig. 1, OBC and LDC are two separate power converters, each of them incorporates a high-frequency transformer to ensure the galvanic isolation between grid and batteries, and the galvanic isolation between high-voltage batteries and low-voltage auxiliary loads. In the OBC, DAB topologies, such as DAB converter [3], series-resonant converter (SRC) [4], and *CLLC* resonant converter [5], are widely adopted. The DAB topologies require additional large inductor to achieve wide range zero-voltage switching (ZVS) of power switches, and the magnetic components account for the major volume and weight of the VCS.

With the increasing demand to extend the driving range of the EVs, the capacities of the HVB have been increasing. In the same time, the intelligence equipment of EVs, such as autonomous driving systems, radars, and smart cockpit systems, have elevated the power level of LDC [6]. Much work has been done to develop high efficiency, high-power-density VCS to reduce charging durations and to adapt to the limited installation space of EVs. Many studies have been focused on integrating the circuit topologies of the OBC and the LDC to reduce the volume, the weight, and the cost of the overall system [7], [8], [9], [10], [11], [12], [13]. A multiwinding transformer structure, as shown in Fig. 2, is used to achieve the integrated VCS, in which active switches and passive components are shared, which effectively reduces the number of semiconductor devices and transformers.

Magnetic integration is an effective way to increase the power density of the integrated VCS. Various works have been reported to integrate the ZVS inductor with the transformer [14], [15], [16], [17], [18], [19], [20], [21], [22], [23]. A simple split-winding transformer structure is proposed to realize the required leakage inductance [14], [15], [16], [17]. However, large leakage inductance leads to large volume of the magnetic core. Furthermore, a huge amount of flux leaks into the external environment, resulting in increased winding losses [18], [19].

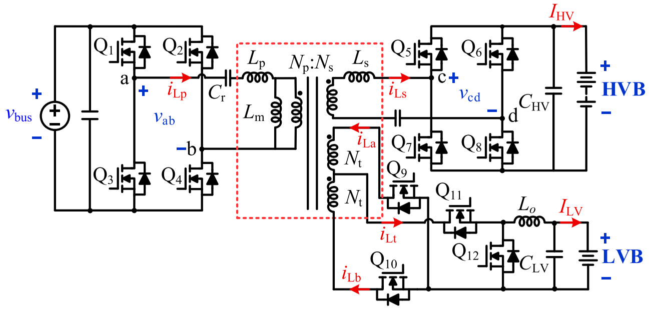

Fig. 2. Circuit topology of the integrated VCS.

The interleaved winding structure used in planar IMC can effectively handle the external leakage flux to reduce the ac resistance [20], [21], [22]. However, it leads to a smaller equivalent leakage inductance, thereby limits its capability to achieve a wide ZVS range. To address these issues, the operating frequency of the IMC is increased to hundred kilohertz to reduce the requirement for the leakage inductance. However, high-frequency planar IMC face significant challenges in integrated VCS.

Due to the low-voltage high-current output of the LDC, the CTR is widely adopted [11], [23], [24], with an additional built-in buck circuit to regulate the induced voltage of the LDC windings, as shown in Fig. 2. The switching frequency of the built-in buck circuit is twice that of the OBC, which leads to higher switching losses of the LDC. In addition, the electromagnetic compatibility (EMC) emission standards for vehicles apply to frequencies ranging from 150 kHz to 960 MHz [25]. High frequencies introduce additional electromagnetic interference (EMI) issues to the system. Moreover, the adjacent PCB winding layers of the planar IMC are prone to higher parasitic capacitance, which further affects the EMC performance.

In the applications with low switching frequency and high-power, the number of the turns of the IMC winding increases, and multilayer PCBs are required to accommodate the turns ratio. Furthermore, multilayer PCBs are needed to meet the current density of the LDC winding. The high cost of multilayer PCBs makes Litz-wire-based IMC more practical for integrated VCS. In [26], a Litz-wire-based IMC for a triple-active-bridge converter is proposed, which integrates the transformer and two external inductors. However, the secondary and the tertiary windings in this structure have identical specifications, which limit its application in the LDC. Copper bars are usually used to achieve sufficient current density in the LDC. However, external leakage flux induces large eddy current losses in the LDC windings, which reduces system efficiency.

In this article, a Litz-wired IMC structure is proposed to integrate the high-frequency transformers of the OBC and the LDC with the resonant inductor of the OBC. Based on the proposed IMC, the system can charge the HVB and the LVB simultaneously. The main contributions of the proposed IMC are summarized as follows.

1) The system operates as an SRC for OBC to charge the HVB. The proposed IMC achieves the integration of the

high-frequency transformer with the resonant inductor of the SRC. An elliptical magnetic shunt is employed to achieve controllable leakage inductance, enabling the SRC to achieve ZVS over a wide output voltage range.

2) The system operates as a full bridge converter for the LDC to charge the LVB. The proposed IMC enables the sharing of the secondary-side H-bridge of the OBC and achieves minimized equivalent leakage inductance of the LDC winding, which reduces the voltage stress on the LDC switching devices.
3) The LDC windings are formed by multistranded Litz wire. Compared to conventional copper bar windings, the proposed structure effectively mitigates eddy current losses from external leakage flux, enabling the LDC winding to deliver high-current output with thermal robustness.
4) A modeling and leakage-inductance design method is developed for the proposed IMC, which takes into account the asymmetric leakage magnetic field and enables the extraction of elliptical-path parameters, simplifying the calculation while maintaining accuracy and designability.

The rest of this article is organized as follows. In Section II, the equivalent circuit model of the multiwinding transformer is investigated. Section III describes the proposed IMC structure, and provides a detailed calculation of the leakage inductance. Section IV presents the design of the proposed IMC for a 6.6 kW integrated VCS. Experimental verification for the proposed IMC is given in Section V. Section VI concludes this article.

II. INVESTIGATION OF MULTIWINDING TRANSFORMER

The multiwinding transformer of the integrated VCS, as shown in Fig. 2, consists of four windings. N_p and N_s are the number of the turns of the primary and the secondary windings of the OBC, N_t is the number of the turns of the LDC winding, respectively. In Fig. 2, by using the multiwinding transformer, the H-bridge of the secondary of the OBC is shared for both the OBC and the LDC. The current in the LDC winding is derived from the secondary current of the OBC.

Fig. 3 shows the equivalent circuit of the multiwinding transformer and its corresponding π model. In each half-switching cycle of the OBC, only one terminal of the LDC winding conducts current. The current direction in the LDC winding is aligned with that of the secondary winding of the OBC. To simplify the transformer model, the multi-winding transformer is equivalent to a three-winding transformer, and the π model [27] is used for analysis.

The circuit equation of the three-winding transformers is as follows:

$$\begin{bmatrix} v_\mathrm{p} \\ v_\mathrm{s} \\ v_\mathrm{t} \end{bmatrix} = \begin{bmatrix} L_\mathrm{pp} & M_\mathrm{ps} & M_\mathrm{pt} \\ M_\mathrm{ps} & L_\mathrm{ss} & M_\mathrm{st} \\ M_\mathrm{pt} & M_\mathrm{st} & L_\mathrm{tt} \end{bmatrix} \begin{bmatrix} di_{L\mathrm{p}}/dt \\ di_{L\mathrm{s}}/dt \\ di_{L\mathrm{t}}/dt \end{bmatrix} \tag{1}$$

where v_k and $i_{L\mathrm{k}}$ ($k = \mathrm{p, s, t}$) are the voltages and currents of the corresponding windings, L_kk is the self-inductance of winding k, and $M_{kj} = M_{jk}$ ($j \neq k$) is the mutual inductance between winding j and winding k.

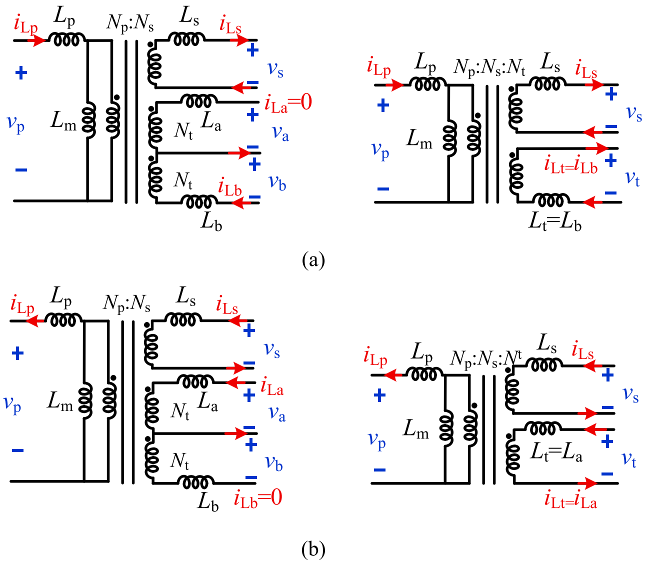

Fig. 3. Equivalent circuit of the multiwinding transformer and its corresponding π-model. (a) In the positive half-switching cycle. (b) In the negative half-switching cycle.

In the π-model, all windings share a common magnetizing flux in the magnetic core, and the inductance matrix $\boldsymbol{L}$ can be expressed as follows:

$$\mathbf{L} = \begin{bmatrix} L_\mathrm{p} & 0 & 0 \\ 0 & L_\mathrm{s} & 0 \\ 0 & 0 & L_\mathrm{t} \end{bmatrix} + L_\mathrm{m} \begin{bmatrix} a_\mathrm{p} \\ a_\mathrm{s} \\ a_\mathrm{t} \end{bmatrix} \begin{bmatrix} a_\mathrm{p} & a_\mathrm{s} & a_\mathrm{t} \end{bmatrix} \tag{2}$$

where L_k ($k = \mathrm{p, s, t}$) are the leakage inductances of the primary, the secondary, and the tertiary windings, respectively. L_m is the magnetizing inductance. a_k ($k = \mathrm{p, s, t}$) are the normalized number of turns; it is defined as $a_\mathrm{k} = N_\mathrm{k}/N_\mathrm{ref}$, where N_ref is the number of turns of the reference winding.

By comparing the inductance matrices in (1) and (2), the following expressions are obtained:

$$\begin{cases} L_\mathrm{pp} = L_\mathrm{p} + a_\mathrm{p}^2 L_\mathrm{m} \\ L_\mathrm{ss} = L_\mathrm{s} + a_\mathrm{s}^2 L_\mathrm{m} \\ L_\mathrm{tt} = L_\mathrm{t} + a_\mathrm{t}^2 L_\mathrm{m} \end{cases}, \quad \begin{cases} M_\mathrm{ps} = a_\mathrm{p} a_\mathrm{s} L_\mathrm{m} \\ M_\mathrm{pt} = a_\mathrm{p} a_t L_\mathrm{m} \\ M_\mathrm{st} = a_\mathrm{s} a_t L_\mathrm{m} \end{cases}. \tag{3}$$

Taking the primary winding as the reference winding, the following expressions are obtained:

$$a_\mathrm{p} = 1,\ a_\mathrm{s} = \frac{M_\mathrm{st}}{M_\mathrm{pt}},\ a_t = \frac{M_\mathrm{st}}{M_\mathrm{ps}}. \tag{4}$$

By substituting (4) into (3), L_k ($k = \mathrm{p, s, t}$) and L_m can be derived as follows:

$$\begin{matrix} L_\mathrm{p} = L_\mathrm{pp} - \frac{M_\mathrm{ps} M_\mathrm{pt}}{M_\mathrm{st}},\ L_\mathrm{s} = L_\mathrm{ss} - \frac{M_\mathrm{ps} M_\mathrm{st}}{M_\mathrm{pt}} \\ L_\mathrm{t} = L_\mathrm{tt} - \frac{M_\mathrm{st} M_\mathrm{pt}}{M_\mathrm{ps}},\ L_\mathrm{m} = \frac{M_\mathrm{ps} M_\mathrm{pt}}{M_\mathrm{st}} \end{matrix}. \tag{5}$$

The inductance matrix in (1) can be extracted through finite-element analysis (FEA). Based on (4)–(5), L_m and L_k ($k = \mathrm{p, s,}$ t) can be calculated. L_m corresponds to the main magnetic path in the core that is shared by all windings, whereas L_k represents the leakage-flux components that are excited by the winding currents but not coupled into the common magnetic flux.

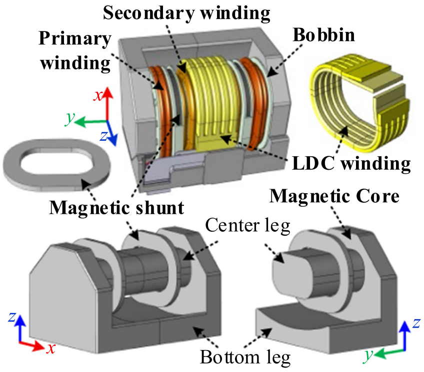

Fig. 4. 3-D structure of the proposed IMC.

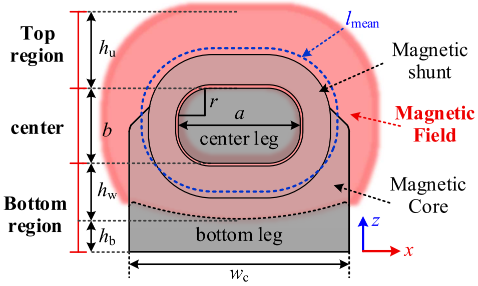

Fig. 5. Magnetic field distribution in x–z plane.

It is worth noting that, in the proposed IMC, the OBC secondary and LDC windings are designed with a high coupling coefficient. The HVB clamps the voltage of the secondary winding through the secondary H-bridge, so that the LDC power is directly supplied from the HVB. Consequently, the equivalent leakage inductance of the OBC can be derived as follows:

$$L_{\mathrm{eq}} = L_{\mathrm{p}} + \left(\frac{M_{\mathrm{pt}}}{M_{\mathrm{st}}}\right)^2 \cdot L_{\mathrm{s}}. \tag{6}$$

III. DESIGN OF THE PROPOSED IMC

A. *Structure of the Proposed IMC*

In this article, a modified URS core structure is employed, in which the center leg is designed with a rounded-rectangular cross section, and its cross-sectional area is approximately equal to that of the bottom leg. Compared with conventional PQ and EE cores, the proposed core features a simple structure and better manufacturability. In addition, its winding arrangement offers a larger exposed surface area, resulting in improved thermal dissipation performance.

Fig. 4 shows the structure of the proposed IMC. In Fig. 4, two elliptical ring-shaped magnetic shunts are symmetrically inserted into the center leg of the magnetic core, and air gaps are formed between each shunt and the center leg. The magnetic shunts are mechanically secured by the bobbin, which ensures accurate positioning and maintains the designed air gap between the shunts and the center leg. The secondary winding of the OBC is centrally wound on the center leg of the core between the two magnetic shunts, while the primary winding is symmetrically wound on both sides. The LDC winding is implemented using multistrands Litz wires, which are concentrically wound with the secondary windings of the OBC.

The leakage inductance of the proposed IMC arises from the leakage flux between the primary and the secondary windings of the OBC. Alternating flux generated by the primary winding within the core is not fully couple with the secondary winding. A portion of the magnetic flux leaks into the surrounding air and returns through the air path.

The magnetic shunt provides a low-reluctance bypass path for the magnetic flux, which further reduces the coupling coefficient between the primary and the secondary windings, and thus increases the equivalent leakage inductance of the IMC. By adjusting the air gap, the geometry and the permeability of the magnetic shunts, the leakage inductance can be tuned within a controllable range.

Assuming the permeability of the magnetic core is significantly high, the total energy stored in the leakage inductance is divided into two parts: the energy stored in the magnetic shunts and the leakage energy associated with the OBC windings.

B. *Energy Stored in the Leakage Inductances*

In order to estimate the leakage energy caused by the leakage flux, the following conditions are assumed.

1) When the secondary winding is short-circuited, the main flux in the core can be negligible, only the leakage magnetic field is present in the core window.
2) At low frequencies, the magnetic field distribution within the core window is not affected by the high-frequency effects of the Litz wire.
3) The windings of the IMC are symmetrically arranged around the center leg, and the magnetic field is primarily concentrated within the elliptical ring-shaped region shown in Fig. 5.

Fig. 5 shows the magnetic field distribution along the x–z plane in Fig. 4. As shown in Fig. 5, as the bottom region of the magnetic core includes a bottom leg while the top region above the center leg is open, the magnetic field in the top region tends to spread more extensively. Therefore, the magnetic energy stored in the top and bottom regions adjacent to the center leg becomes asymmetric. To simplify the analysis, the vertical distance of the top region h_{u} is defined as follows:

$$h_{\mathrm{u}} = h_{\mathrm{w}} + h_{\mathrm{b}}/2 \tag{7}$$

where h_{w} and h_{b} are the height of the core window and the bottom leg, respectively.

In Fig. 5, l_{mean} represents the effective magnetic path length of the leakage flux and is approximated as a rounded-rectangle closed path. The length in the x-direction is $a - 2r$, and the length in the z-direction is $b - 2r$. Each corner is modeled as a quarter arc with a radius of $R = (h_{\mathrm{u}} + h_{\mathrm{w}})/4 + r$. Thus, l_{mean} can be approximately expressed as follows:

$$l_{\mathrm{mean}} \approx 2\pi \cdot \left(\frac{h_{\mathrm{u}} + h_{\mathrm{w}}}{4} + r\right) + 2\left(a + b - 4r\right) \tag{8}$$

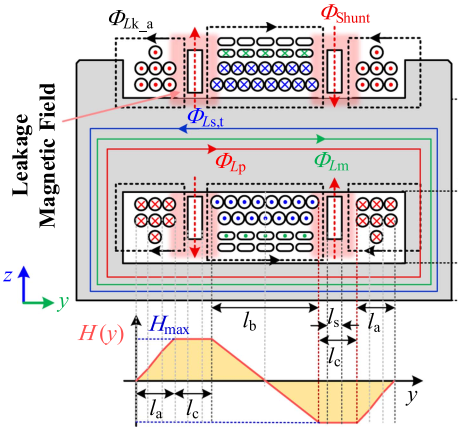

Fig. 6. Magnetic flux distribution and magnetic field intensity distribution in y–z plane of the proposed IMC.

where r is the chamfer radius of the center leg, and a and b are its length and height, respectively.

Fig. 6 shows the distributions of the magnetic flux and the magnetic field intensity along the y--z plane in Fig. 4. Φ_{Lp} is the flux paths from the primary windings, $\Phi_{\mathrm{Ls,t}}$ is the flux paths from the OBC secondary and LDC windings, and $\Phi_{\mathrm{Lk{\cdot}a}}$ is the leakage flux paths within the air, and Φ_{Shunt} is the leakage flux paths through the magnetic shunts. The total leakage flux Φ_{Lk} is quantified as the sum of $\Phi_{\mathrm{Lk{\cdot}a}}$ and Φ_{Shunt}.

According to above assumptions and based on Ampere's circuital law, the magnetic field intensity within the core window can be obtained as follows:

$$H_{\mathrm{s}} = \frac{N_{\mathrm{Litz}} I_{\mathrm{b}}}{h_{\mathrm{w}}} \tag{9}$$

where N_{Litz} is the equivalent number of turns of the Litz wire winding, and I_{b} is the winding current of OBC.

In the proposed IMC, the windings are symmetrically arranged around the center leg, so that the magnetic field intensity distributions on both sides are approximately identical. According to (9), the y–z plane shown in Fig. 6 can be divided into several regions that contribute to the leakage magnetic energy.

The magnetic field intensity distribution within the core window can be approximated by a piecewise linear model, which can be expressed as follows:

$$H(y) = \begin{cases} H_{\max}\frac{y}{l_{\mathrm{a}}} & 0 < y \le l_{\mathrm{a}} \\ H_{\max} & l_{\mathrm{a}} < y \le l_{\mathrm{a}} + l_{\mathrm{c}} \\ H_{\max}\left(1 - \frac{y - l_{\mathrm{a}} - l_{\mathrm{c}}}{l_{\mathrm{b}}/2}\right) & l_{\mathrm{a}} + l_{\mathrm{c}} < y \le l_{\mathrm{b}}/2 \end{cases} \tag{10}$$

where $H_{\max} = N_{\mathrm{p}} I_{\mathrm{pmax}}/(2h_{\mathrm{w}})$ is the maximum magnetic field intensity, l_{a} is the width of the primary winding, l_{b} is the width of the secondary winding, and l_{c} is the spacing between the primary and secondary windings.

The leakage energy stored in the air can be calculated by integral calculation

$$E_{\mathrm{air}} = \frac{1}{2}\iiint_V BH dV = \frac{1}{2}\mu_0 l_{\mathrm{mean}} h_{\mathrm{w}} \int H^2 dy \tag{11}$$

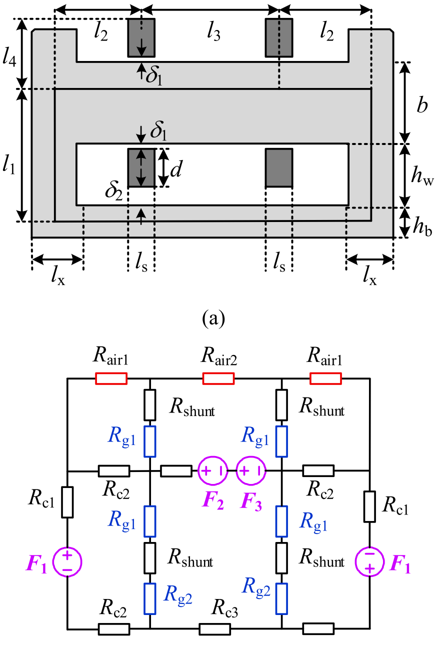

(a)

(b)

Fig. 7. Proposed IMC structure. (a) Geometry in y–z plane. (b) Reluctance model.

where V is the total volume of window area, μ_0 is the magnetic permeability of air, B is the flux density, H is the magnetic field intensity, and l_{mean} is the effective magnetic path length.

The energy stored in each region can be calculated using (10) and (11), and the total leakage energy is obtained by summing these components, which can be expressed as follows:

$$E_{\mathrm{air}} = \frac{\mu_0 l_{\mathrm{mean}} N_{\mathrm{p}}^2 I_{\mathrm{p}}^2}{24 h_{\mathrm{w}}}\left(2l_{\mathrm{a}} + l_{\mathrm{b}} + 6l_{\mathrm{c}}\right). \tag{12}$$

By transferring the leakage inductance to the primary side of the OBC, the equivalent leakage inductance is expressed as follows:

$$L_{k\mathrm{p\_air}} = \frac{2E_{\mathrm{air}}}{I_{\mathrm{p}}^2} = \frac{\mu_0 l_{\mathrm{mean}} N_{\mathrm{p}}^2}{12 h_{\mathrm{w}}}\left(2l_{\mathrm{a}} + l_{\mathrm{b}} + 6l_{\mathrm{c}}\right). \tag{13}$$

C. Energy Stored in the Magnetic Shunts

Fig. 7(a) shows the geometry and the dimensions of the proposed IMC. Two elliptical ring-shaped magnetic shunts are inserted into the center leg of the magnetic core, with an air gap δ_1 between the inner ring of each shunt and the center leg. An additional air gap δ_2 exists between the outer ring of each shunt and the bottom leg of the magnetic core.

Fig. 7(b) shows the reluctance model of the proposed IMC. R_{c1}, R_{c2} and R_{c3} are the internal reluctances of the magnetic core, R_{shunt} is the reluctance of the magnetic shunt, R_{g1} and R_{g2} are the air-gap reluctance of the magnetic shunt. The air-gap reluctance R_{air1} and R_{air2} are established between the outer ring of the shunts and the air. F_1, F_2, and F_3 are the magnetomotive forces.

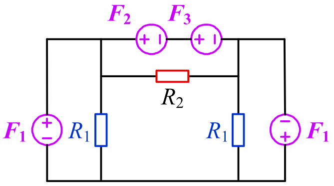

Fig. 8. Simplified reluctance model.

Assuming the permeability of the core is significantly higher than the permeability of air, i.e., $\mu_{\text{c}} >> \mu_0$. Consequently, only the reluctance of air-gap is considered, and the simplified reluctance model is shown in Fig. 8.

The reluctances of the air-gap are derived as follows:

$$\begin{aligned} R_{\text{g1}} &= \frac{\delta_1}{\mu_0 \cdot l_{\text{s}} C_1}, R_{\text{g2}} = \frac{\delta_2}{\mu_0 \cdot l_{\text{s}} C_2}, \\ R_{\text{air1}} &= \frac{l_2}{\mu_0 \cdot l_{\text{s}} C_2}, R_{\text{air2}} = \frac{l_3}{\mu_0 \cdot l_{\text{s}} C_2} \end{aligned} \tag{14}$$

where C_1 is half the circumference of the inner ring of the shunt, and C_2 is half the circumference of the outer ring.

The simplified reluctance in Fig. 8 is obtained as follows:

$$R_1 = R_{\text{g1}} + R_{\text{g2}},\ R_2 = 2\left(R_{\text{air1}} // R_{\text{g1}}\right) + R_{\text{air2}}. \tag{15}$$

According to Faraday-Lenz's law as given in the following:

$$v\left(t\right) = N\frac{d\Phi\left(t\right)}{dt} = L\frac{di\left(t\right)}{dt}. \tag{16}$$

The leakage inductance L_{p}, L_{s}, and L_{t} of the three-winding transformer can be expressed as follows:

$$L_{\text{p}} = \frac{N_{\text{p}}^2}{R_1},\ L_{\text{s}} = \frac{N_{\text{s}}^2}{R_2},\ L_{\text{t}} = \frac{N_{\text{t}}^2}{R_2}. \tag{17}$$

From (6) and (17), the equivalent leakage inductance can be calculated as follows:

$$L_{\text{kp\_shunt}} = L_{\text{p}} + \left(\frac{N_{\text{p}}}{N_{\text{s}}}\right)^2 L_{\text{s}}. \tag{18}$$

The energy stored in the shunts can be expressed as follows:

$$E_{\text{shunt}} = \frac{1}{2} L_{\text{kp\_shunt}} I_{\text{p}}^2. \tag{19}$$

The total equivalent leakage inductance of the proposed IMC can be calculated as follows:

$$L_{\text{k\_total}} = L_{\text{kp\_air}} + L_{\text{kp\_shunt}}. \tag{20}$$

D. Design of the Magnetic Shunts

In Fig. 6, the leakage flux in the region of the magnetic shunt can be derived as follows:

$$\Phi_{\text{s\_air}} \approx \int_0^{l_{\text{c}}} \left(\mu_0 H_{\text{s}} l_{\text{mean}}\right) dx = \frac{\mu_0 l_{\text{c}} l_{\text{mean}} N_{\text{P}} I_{\text{P}}}{2h_{\text{w}}}. \tag{21}$$

In Fig. 8, the leakage inductance flux of a single magnetic shunt can be derived as follows:

$$\Phi_{\text{shunt}} = \frac{F_1}{R_1} = \frac{\mu_0 l_{\text{s}} C_1 C_2 N_{\text{P}} I_{\text{P}}}{2\left(\delta_1 C_2 + \delta_2 C_1\right)}. \tag{22}$$

Assuming the magnetic field intensity within the air gaps between the magnetic shunt and the center leg is uniform. The maximum flux density of the magnetic shunt is defined as follows:

$$B_{\text{max\_shunt}} = \frac{\Phi_{\text{max}}}{A_{\text{e\_shunt}}} = \frac{\Phi_{\text{shunt\_max}} + \Phi_{\text{s\_air\_max}}}{l_{\text{s}} \cdot C_{\text{s}}} \tag{23}$$

where $A_{\text{e}\cdot\text{shunt}}$ and C_{s} are the cross-sectional area and the equivalent half-circumference of the magnetic shunt.

From (21), (22), and (23), the following equations can be obtained:

$$\frac{\delta_1}{C_1} + \frac{\delta_2}{C_2} = \left(\frac{2C_{\text{s}} B_{\text{max\_shunt}}}{\mu_0 N_{\text{P}} I_{\text{Pmax}}} - \frac{l_{\text{c}} l_{\text{mean}}}{h_{\text{w}} l_{\text{s}}}\right)^{-1} \tag{24}$$

where I_{pmax} is the peak current of the primary winding.

From (17), (22), and (23), the average cross-sectional area of a single magnetic shunts can be approximately expressed as follows:

$$A_{\text{e\_shunt}} \approx \frac{L_k I_{\text{Pmax}}}{2N_{\text{P}} B_{\text{max\_shunt}}} \tag{25}$$

Based on the above analysis, the leakage inductance of the IMC can be effectively regulated by the design of the dimensions and the air gap of the magnetic shunt. The magnetic shunt features a relatively small inner cross-sectional area, leading to a high maximum flux density. As C_{s} increases, the flux density within the magnetic shunt decreases accordingly.

IV. DESIGN OF THE PROPOSED IMC STRUCTURE FOR A 6.6 KW VEHICLE CHARGING SYSTEM

In order to validate the proposed IMC structure, a 6.6 kW integrated VCS is designed, with the circuit topology shown in Fig. 2. The voltage range of the HVB and the LVB are from 250 to 500 V, and from 9 to 16 V, respectively. The number of the turns of N_{t} is fixed at 1 to reduce the conduction losses. The maximum duty cycle of the LDC is set to $D_{\max} = 85\%$, and the number of the turns of N_{p} and N_{s} are obtained as follows:

$$N_{\text{s}} \leq \frac{V_{\text{HVmin}} \cdot N_{\text{t}}}{V_{\text{LVmax}}} \cdot D_{\max},\ N_{\text{p}} \leq \frac{k_{\max} V_{\text{busmax}} N_{\text{s}}}{V_{\text{HVmax}}} \tag{26}$$

where V_{HVmin} is the minimum output voltage of the OBC, V_{LVmax} is the maximum output voltage of the LDC, and $k_{\max}$ is the maximum voltage conversion ratio of the OBC.

A. Design of the Resonant Tank

The parameters of the resonant tank are crucial in the design of the SRC converter. In this article, all parameters of the SRC are transferred to primary side. The following normalized base values are selected: $V_{\text{B}} = V_{\text{bus}}$, $Z_{\text{B}} = n^2 {V_{\text{HV}}}^2 / P_{\text{o}}$, and $I_{\text{B}} = V_{\text{B}} / Z_{\text{B}}$. The voltage gain is defined as $k = nV_{\text{HV}} / V_{\text{bus}}$.

Based on the normalized base values, the normalized output power can be expressed as follows:

$$P_{\text{o,pu}} = \frac{1}{V_{\text{B}} I_{\text{B}}} \cdot \frac{n^2 V_{\text{HV}}^2}{Z_{\text{B}}} = \frac{k^2 V_{\text{bus}}^2}{V_{\text{B}}^2} = k^2. \tag{27}$$

The normalized switching frequency is expressed as follows:

$$F = \frac{\omega_{\text{s}}}{\omega_{\text{r}}} = \frac{f_{\text{s}}}{f_{\text{r}}},\ f_r = \frac{1}{2\pi\sqrt{L_{\text{r}} C_{\text{r}}}} \tag{28}$$

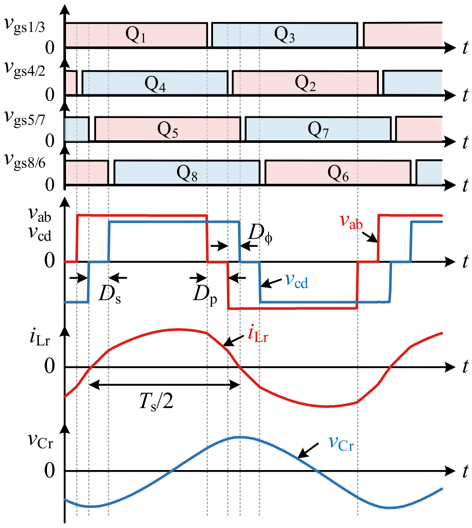

Fig. 9. Key waveforms of the resonant tank.

where f_r is the resonant frequency and $f_s = 1/T_s$ is the switching frequency of the OBC, L_r is the resonant inductance and C_r is the resonant capacitance.

The normalized reactance is expressed as follows:

$$X_{r,pu} = Q\left(F - \frac{1}{F}\right), Q = \frac{\omega_r L_r}{Z_B} \tag{29}$$

where Q is the quality factor.

Fig. 9 shows the key waveforms of the resonant tank. D_p and D_s are the internal phase shift duty cycle of Q_3 and Q_2, as well as Q_7 and Q_6, respectively. D_ϕ is the phase shift duty cycle of Q_2 and Q_7. By controlling D_p and D_s, the primary bridge voltage $v_{ab}(t)$ and the secondary bridge voltage v_{cd}(t) are generated. The selection of D_p and D_s is directly influenced by the voltage gain k and the output power P_o. When $k < 1$, D_p modulation is applied on the primary side, whereas when $k > 1$, D_s modulation is applied on the secondary side. Under light-load conditions, both D_p and D_s modulations are applied simultaneously, which is referred to as TPS modulation.

The external phase-shift duty cycle D_f represents the phase shift between $v_{ab}(t)$ and v_{cd} (t), and is defined as $D_f = D_p/2 + D_s/2 + D_\phi$. D_f determines the direction of the power flow: $D_f > 0$ corresponds to the mode where the high-voltage battery is charged. In this mode, the fundamental components of the resonant current and the bridge voltages are the main contributors to the transferred power.

In order to simplify the analysis, the fundamental harmonic approximation method is used. The normalized bridge voltages $v_{ab,pu}(t)$ and $v_{cd,pu}(t)$, and the normalized current of the resonant tank $i_{Lr,pu}$ can be derived as follows:

$$\begin{aligned} v_{ab,pu}(t) &= \tfrac{4}{\pi}\cos\alpha_p \sin(\omega_s t) \\ v_{cd,pu}(t) &= \tfrac{4k}{\pi}\cos\alpha_s \sin(\omega_s t - \theta) \end{aligned} \tag{30}$$

$$\begin{aligned} &i_{Lr,pu}(t) \\ &= \tfrac{4}{\pi X_{r,pu}}\left(-\cos\alpha_p \cos(\omega_s t) + k\cos\alpha_s \cos(\omega_s t - \theta)\right) \end{aligned} \tag{31}$$

where $\alpha_p = D_p\pi/2$, $\alpha_s = D_s\pi/2$, $\theta = D_f\pi$.

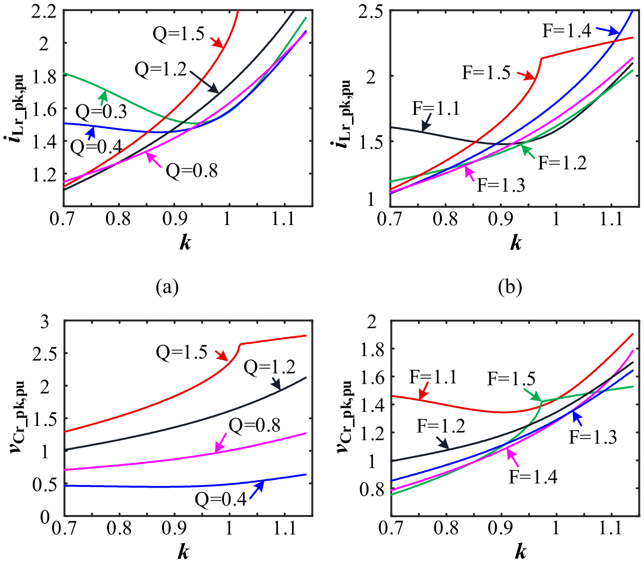

(a) (b)

(c) (d)

Fig. 10. Variations of the peak voltage of tank capacitor and the peak current of resonant tank. (a) Normalized peak current for different Q, with $F = 1.3$. (b) Normalized peak current for different F, with $Q = 1$. (c) Normalized peak voltage for different Q, with $F = 1.3$. (d) Normalized peak voltage for different F, with $Q = 1$.

The normalized peak resonant inductor current and the normalized peak voltage of the tank capacitor are derived as follows:

$$\begin{aligned} &i_{Lr\_pk,pu} = \\ &\tfrac{4}{\pi X_{r,pu}}\sqrt{\left(k\cos\alpha_s\cos\theta - \cos\alpha_p\right)^2 + \left(k\cos\alpha_s\sin\theta\right)^2} \end{aligned} \tag{32}$$

$$\begin{aligned} &v_{Cr\_pk,pu} = \\ &\tfrac{4}{\pi(F^2-1)}\sqrt{\cos^2\alpha_p + k^2\cos^2\alpha_s - 2k\,\cos\alpha_p\cos\alpha_s\cos\theta}. \end{aligned} \tag{33}$$

The normalized average output power of the OBC can be derived using the primary-side bridge voltage $v_{ab,pu}(t)$ and tank current $i_{Lr,pu}(t)$ as follows:

$$\begin{aligned} P_{o,pu} &= \tfrac{1}{2\pi}\int_0^{2\pi} v_{ab,pu}(t)\cdot i_{Lr,pu}(t)\,d(\omega_s t) \\ &= \tfrac{8k}{\pi^2 X_{r,pu}} cos\alpha_s cos\alpha_p sin\theta \end{aligned}. \tag{34}$$

It can be seen from (32)–(34) that the parameters k, F, and Q are crucial for the design of the tank parameters. To verify the impact of the parameters F and Q on the resonant tank, the variations of the peak voltage of the tank capacitor and the peak resonant tank current with respect to k are plotted under full load conditions for different Q and F, as shown in Fig. 10.

It can be known from Fig. 10 that, in order to reduce the peak current of the resonant tank, Q should be higher when k is small, while Q should decrease with the increase of k. The peak voltage of the resonant capacitor increases with the increase of Q, whereas higher F helps to reduce the peak voltage. From (29), Q decreases with the increase of k, and Q can thus be determined based on the minimum output voltage of the OBC.

It is designed to have $Q = 0.8$ and $F = 1.3$–1.4 under the full load with the voltage of the HVB is 300 V. This ensures that the resonant tank operates in the inductive region, which is beneficial to achieve ZVS and reduce the peak current of the resonant tank. The switching frequency of the OBC is set to 100 kHz to achieve a tradeoff between switching losses and conduction losses, and to meet EMI requirements and aligns well with the characteristics of ferrite magnetic materials.

Therefore, the parameters of the resonant tank are as follows:

$$L_r = QF\frac{Z_{\mathrm{B}}}{\omega_s},\ C_r = \frac{F}{Q}\frac{1}{\omega_s Z_{\mathrm{B}}}. \tag{35}$$

To improve the charging efficiency, the parameters of the resonant tank should be optimized to ensure ZVS over a wide voltage range of the HVB under the full load condition. In this article, minimum resonant current algorithm [28] is adopted, and the inner phase-shift angle is given by the following:

$$\begin{cases} \alpha_{\mathrm{p}} = \cos^{-1}\left(\frac{k}{\cos\theta}\right), \alpha_{\mathrm{s}} = 0 & k < 1 \\ \alpha_{\mathrm{p}} = 0,\ \alpha_{\mathrm{s}} = 0 & k = 1\, . \\ \alpha_{\mathrm{s}} = \cos^{-1}\left(\frac{1}{k\cos\theta}\right), \alpha_{\mathrm{p}} = 0 & k > 1 \end{cases} \tag{36}$$

The conditions to achieve ZVS operation can be derived as follows:

$$\begin{cases} \alpha_{\mathrm{p}} \le \sin^{-1}\sqrt{1-k} \le \theta \le \cos^{-1}k & k < 1 \\ \alpha_s \le \sin^{-1}\sqrt{1-\frac{1}{k}} \le \theta \le \cos^{-1}\frac{1}{k} & k > 1 \end{cases}. \tag{37}$$

From (27), (34), and (36), the external phase-shift angle corresponding to the given power can be expressed as follows:

$$\theta = \begin{cases} \arctan\left(\frac{\pi^2}{8}X_{\mathrm{r,pu}}\right) & k < 1, \theta < \cos^{-1}(k) \\ \arctan\left(\frac{k^2\pi^2}{8}X_{\mathrm{r,pu}}\right) & k > 1, \theta < \cos^{-1}\left(\frac{1}{k}\right) \end{cases}. \tag{38}$$

The equivalent impedance of the resonant tank at the operating angular frequency ω_{s} is defined as $Z_{\mathrm{eff}} = \omega_{\mathrm{s}}L_{\mathrm{r}}$ - $1/(\omega_{\mathrm{s}}C_{\mathrm{r}})$, and the normalized reactance can be expressed as follows:

$$X_{\mathrm{r,pu}} = \frac{P_{\mathrm{o}}}{n^2V_{\mathrm{HV}}^2}\left(\omega_{\mathrm{s}}L_{\mathrm{r}} - \frac{1}{\omega_{\mathrm{s}}C_{\mathrm{r}}}\right) = \frac{Z_{\mathrm{eff}}}{Z_{\mathrm{B}}}. \tag{39}$$

By properly designing Z_{eff}, the maximum external phase-shift angle θ at the rated power is constrained to $\pi/4$, which helps reduce the reactive power of the system. From (36)–(39), the ZVS condition required for operation with the minimum resonant current can be expressed as follows:

$$\begin{cases} \frac{8Z_{\mathrm{B}}}{\pi^2}\sqrt{\frac{1-k}{k}} \le Z_{\mathrm{eff}} \le \frac{8Z_{\mathrm{B}}}{\pi^2} & k < 1 \\ 0 \le Z_{\mathrm{eff}} \le \frac{8Z_{\mathrm{B}}}{\pi^2} & k = 1. \\ \frac{8Z_{\mathrm{B}}}{\pi^2}\frac{\sqrt{k-1}}{k^2} \le Z_{\mathrm{eff}} \le \frac{8Z_{\mathrm{B}}}{k^2\pi^2} & k > 1 \end{cases} \tag{40}$$

Based on (35), the initial values of L_{r} and C_{r} can be obtained, and the corresponding Z_{eff} can be calculated. Then, according to (40), L_{r} and C_{r} are further adjusted to achieve ZVS over a wide voltage range of the HVB. By combining (35), (36) and (40), a proper trade-off among ZVS, the RMS current, and the peak current of the resonant tank can be achieved, thereby minimizing the overall system loss. As a result, the resonant parameters are finally designed as $L_{\mathrm{r}} = 20\ \mu$H and $C_{\mathrm{r}} = 230$ nF.

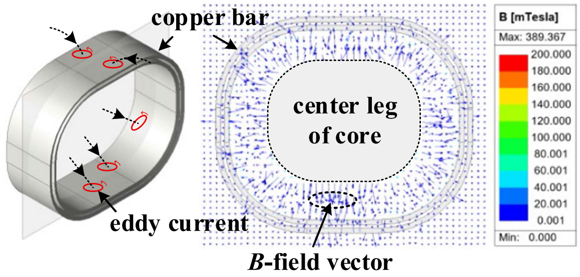

Fig. 11. Vector distribution of magnetic flux density in *x*–*z* plane.

B. Design of the Proposed IMC

The effective cross-sectional area $A_{\mathrm{e}\cdot\mathrm{core}}$ of the proposed IMC is designed based on the assumption that the IMC operates under the worst-case conditions, with a maximum operating flux density $B_{\max}$ set to 200 mT. Therefore, $A_{\mathrm{e}\cdot\mathrm{core}}$ can be calculated as follows:

$$A_{\mathrm{e\_core}} = \frac{V_{\mathrm{HVmax}}}{4f_{\mathrm{s}}N_{\mathrm{s}}B_{\max}} = 416\mathrm{mm}^2 \tag{41}$$

where V_{HVmax} is the maximum output voltage of the OBC.

As the LDC winding is exposed to a three-dimensional time-varying magnetic field generated by the conduction currents of the OBC windings, the skin and internal proximity effects become prominent when conventional copper bars are used for the LDC winding, which significantly increases the winding losses. Moreover, eddy currents induced by external leakage flux, as shown in Fig. 11, contribute to additional temperature rise in the copper bars.

The ac resistance factor $F_{\mathrm{ac,bar}}$ of the copper bars can be obtained by Dowell model [29]

$$F_{\mathrm{ac,bar}} = \Delta\left(\frac{\sinh(2\Delta)+\sin(2\Delta)}{\cosh(2\Delta)-\cos(2\Delta)} + \alpha\cdot\frac{\sinh(\Delta)-\sin(\Delta)}{\cosh(\Delta)+\cos(\Delta)}\right) \tag{42}$$

$$\alpha = \frac{2(m^2-1)}{3}, \Delta = \frac{d_{\mathrm{c}}}{\delta}, R_{\mathrm{dc,bar}} = \frac{MLT_{\mathrm{bar}}}{\sigma\cdot d_{\mathrm{c}}l_{\mathrm{w}}} \tag{43}$$

where d_{c} is the thickness of the copper bar, l_{w} is the width of the copper bar, σ is the electrical conductivity, δ is the skin depth, for a given frequency $f_{\mathrm{s}} = 100$ kHz, $\delta = 0.209$ mm.

To reduce the copper losses, all windings of the proposed IMC are wound using Litz wire. The Litz wire consists of N_0 twisted strands of radius r_0, and the diameter of each strand is smaller than skin depth δ. The LDC windings are formed by multistrands of Litz wire, and their ac resistance factor $F_{\mathrm{ac,Litz}}$ can be calculated using the Tourkhani model [30], [31] and can be expressed as follows:

$$F_{\mathrm{ac,Litz}} = 1 + \frac{\pi^2N_0\beta}{3\cdot 2^6}\left(16m^2 - 1 + \frac{24}{\pi^2}\right)\left(\frac{r_0}{\delta}\right)^4 \tag{44}$$

$$R_{\mathrm{dc,Litz}} = \frac{\mathrm{MLT}_{\mathrm{Litz}}\cdot N}{\pi\cdot\sigma r_0^2N_0} \tag{45}$$

where $\mathrm{MLT}_{\mathrm{Litz}}$ is the mean length per turn of the winding, N is the total number of turns, β is the fill factor, and m is the layers of LDC winding.

In Fig. 11, larger dimensions of copper bar tend to induce wide-area eddy current loops within the conductor, resulting in significant eddy-current losses. In contrast, Litz wire consists of individually insulated fine strands, which prevent the formation of large closed-loop eddy currents. As a result, only small localized eddy currents may be induced within the limited cross-sectional area of each strand.

The additional eddy current dissipation per unit length in Litz wire induced by the surrounding leakage magnetic field H can refer to study [31]

$$P_{\mathrm{eddy\_Litz}} = -N_0 \frac{2\sqrt{2}\pi\rho r_0}{\delta} H^2 \psi_2(\zeta), \zeta = \frac{2r_0}{\delta} \tag{46}$$

where H is the magnetic field intensity, ψ_2 is a dimensionless function determined by ξ, when $r_0 < \delta$, ψ_2 can be approximated by the first term of its Taylor series expansion, expressed as follows:

$$\psi_2(\zeta) = \frac{1}{\sqrt{2}} \left(-\frac{1}{2^5}\zeta^3 + \frac{1}{2^{12}}\zeta^7 + \ldots \right) \approx -\frac{\sqrt{2}}{2^3} \left(\frac{r_0}{\delta} \right)^3. \tag{47}$$

Substituting (47) into (46) yields

$$P_{\mathrm{eddy\_Litz}} \approx \frac{1}{2} \frac{\pi}{\sigma \mu_0^2 \delta^4} \cdot B^2 \cdot N_0 \cdot r_0^4. \tag{48}$$

Under the same magnetic flux density B, switching frequency f, with the copper-bar thickness $d_{\mathrm{c}} << \delta$, the eddy-current loss per unit length of the copper bar can be expressed as follows:

$$P_{\mathrm{eddy\_bar}} = \frac{\pi^2}{6\rho} B^2 f^2 l_{\mathrm{w}} d_{\mathrm{c}}^3 = \frac{1}{6} \frac{B^2}{\sigma \mu_0^2 \delta^4} l_{\mathrm{w}} d_{\mathrm{c}}^3 \tag{49}$$

where l_{w} is the width of the copper bar, and d_{c} is the thickness of the copper bar.

From (48) and (49), the ratio of the eddy-current loss of the copper bar to that of the Litz wire can be expressed as follows:

$$R_{\mathrm{e}} = \frac{P_{\mathrm{eddy\_bar}}}{P_{\mathrm{eddy\_Litz}}} = \frac{l_{\mathrm{w}} d_c^3}{3\pi \cdot N_0 \cdot r_0^4}. \tag{50}$$

The $d_{\mathrm{c}}{}^3$ term in (50) indicates that the eddy-current loss of the copper bar is sensitive to its thickness under the external leakage magnetic field. Since the actual thickness of the copper bar is greater than the skin depth δ, the eddy-current loss in the copper-bar winding becomes significant.

From (48), the additional ac loss induced by the external leakage magnetic field is proportional to $r_0{}^4 \cdot N_0$. A smaller r_0 can effectively reduce the eddy current loss. Therefore, the wire diameter of the Litz strands is selected as $r_0 = 0.025$ mm in this work. The number of strands is determined based on the allowable current density

$$N_0 = \frac{I_{\mathrm{rms}}}{N \cdot J_{\mathrm{A}} \pi r_0^2} \tag{51}$$

where J_{A} is the current density of the LDC winding, and I_{rms} is the RMS current flowing through the winding.

TABLE I
KEY SPECIFICATIONS OF THE PROPOSED IMC

Symbol	Value	Symbol	Value
w_{c}	49 mm	δ_1	1.3 mm
h_{w}	12.8 mm	δ_2	4.8 mm
l_{a}	8.5 mm	C_1	41 mm
l_{b}	23.3 mm	C_2	62 mm
l_{c}	5 mm	l_2	15 mm
l_{s}	2.4 mm	l_3	30 mm
a	27 mm	h_{b}	7 mm
b	17 mm	r	7 mm

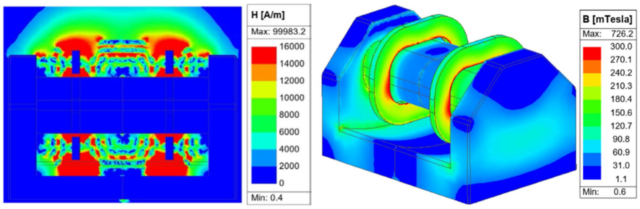

(a) (b)

Fig. 12. FEA simulation of the proposed IMC when $f_{\mathrm{s}} = 100$ kHz, $V_{\mathrm{HV}} = 300$ V, $i_{\mathrm{Lp}} = 36.43$ A, and $i_{\mathrm{Ls}} = 33.89$ A. (a) Magnetic field intensity distribution. (b) Magnetic flux density distribution.

Considering the alternating operation of the LDC winding, I_{rms} is set to 50 A. To meet this requirement, a multistrand Litz wire composed of $N_0 = 1000$ strands and arranged in $N = 4$ parallel bundles is selected. The Litz wire consists of twisted 2UEW/180 enameled strands and wrapped with a single layer of polyimide tape, providing a thermal rating of 180 °C.

From (42)–(45), the ratio of ac resistance between copper bar and Litz wire for the LDC winding is given by the following:

$$F_{\mathrm{ac}} = \frac{F_{\mathrm{ac,bar}} \cdot R_{\mathrm{dc,bar}}}{F_{\mathrm{ac,Litz}} \cdot R_{\mathrm{dc,Litz}}} = 4.17 \tag{52}$$

and the main parameters are as follows: $d_{\mathrm{c}} = 1$ mm, $l_{\mathrm{w}} = 22$ mm, $\beta = 0.35$, $m = 2$, $\mathrm{MLT}_{\mathrm{bar}} = \mathrm{MLT}_{\mathrm{Litz}} = 0.13$ m.

It can be known from (52) that ac resistance of the copper bar is larger than that of the Litz wire, which indicates that using Litz wire for the LDC winding can effectively reduce copper losses caused by high-frequency effects.

With the parameters r_0 and N_0 of the Litz wire determined, the core window area is designed based on turns ratio of the IMC and the outer diameter of the Litz bundle, thereby defining the core dimensions. As analyzed in Section III, the magnetic shunt is dimensioned to achieve the desired leakage inductance. The key specifications of the proposed IMC are given in Table I. The leakage inductance attributed to the leakage energy is approximately 13 μH. Therefore, the magnetic shunt is designed to contribute an additional 7 μH, yielding a total leakage inductance of 20 μH.

To verify the effectiveness of the proposed IMC, Figs. 12 and 13 show the FEA simulation results using Ansys Maxwell under different current conditions.

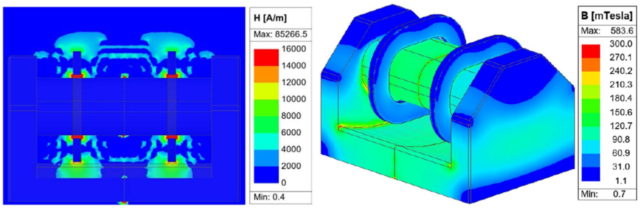

(a) (b)

Fig. 13. FEA simulation of the proposed IMC when $f_{\mathrm{s}} = 100$ kHz, $V_{\mathrm{HV}} = 300$ V, $i_{\mathrm{Lp}} = -7.75$ A, $i_{\mathrm{Ls}} = -7.56$ A. (a) Magnetic field intensity distribution. (b) Magnetic flux density distribution.

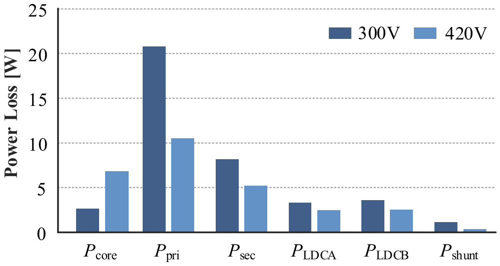

Fig. 14. Loss breakdown of the proposed IMC at the full load.

In Fig. 12, under the condition of maximum resonant current, the magnetic field strength in the shunt region reaches its peak, as described in (9), resulting in non-negligible eddy current losses in the nearby windings. From (22), the magnetic flux density in the shunt also reaches its maximum under this condition, remaining below 300 mT based on the proposed design specifications.

In Fig. 13, under the condition of maximum magnetizing current, the magnetic field strength in the shunt region significantly decreases as the winding current is reduced, leading to a lower magnetic flux density in the shunt. The magnetic core of the IMC reaches its peak flux density under this condition, which remains below 200 mT according to the designed core specifications.

C. Loss Analysis of the Proposed IMC

In this article, TPG33B Mn-Zn ferrite from TDG is selected due to its low core loss density in the 50–150 kHz frequency range, adequate saturation flux density for high-current operation, and reliable thermal stability over the automotive temperature range.

The magnetic core losses of the IMC can be calculated using the original Steinmetz equation (OSE) as follows:

$$P_{\mathrm{core}} = k f^{\alpha} B_{\mathrm{m}}^{\beta} \left(c_{\mathrm{T2}} \tau_{\mathrm{ope}}^{2} - c_{\mathrm{T1}} \tau_{\mathrm{ope}} + c_{\mathrm{T0}} \right) \cdot V_{c} \tag{53}$$

where k, α, and β are determined by fitting the loss density curves provided in the core material datasheet, B_{m} is the maximum flux density of the magnetic core, f is the operating frequency of the transformer, and V_{c} corresponds to the effective core volume.

For the TPG33B material at 100 °C, the fitted coefficients are $k = 5.198 \times 10^{-9}$, $\alpha = 2.143$, and $\beta = 2.813$. The temperature correction term of the OSE can be determined by fitting the loss density-temperature curve under the condition of 100 kHz, and the fitted coefficients are $\mathrm{c}_{\mathrm{T0}} = 0.375$, $c_{\mathrm{T1}} = 2.885 \times 10^{-3}$, and $c_{\mathrm{T2}} = 3.031 \times 10^{-5}$. The normalized temperature correction term is expressed as follows:

$$F_{\mathrm{T}}(T) = \frac{c_{\mathrm{T2}}}{\Delta_{100}} \tau_{\mathrm{ope}}^{2} - \frac{c_{\mathrm{T1}}}{\Delta_{100}} \tau_{\mathrm{ope}} + \frac{c_{\mathrm{T0}}}{\Delta_{100}} \tag{54}$$

where $\Delta_{100} = \mathrm{c}_{\mathrm{T2}} \times 100^{2}$ - $\mathrm{c}_{\mathrm{T1}} \times 100+$ $\mathrm{c}_{\mathrm{T1}} = 0.3874$ kW/m^{3}.

From (31), the magnetic flux density is expressed as follows:

$$B_{1}(t) = \frac{1}{N_{\mathrm{s}} A_{\mathrm{e}}} \int v_{\mathrm{cd}}(t) dt = \frac{4 V_{\mathrm{HV}}}{\pi \omega_{\mathrm{s}} N_{\mathrm{s}} A_{\mathrm{e}}} \left| \cos\left(\alpha_{\mathrm{s}} \right) \right| \tag{55}$$

where N_{s} is the number of turns of the secondary-side, and A_{e} is the effective core cross-sectional area.

From (44) and (45), the winding loss can be calculated as follows:

$$P_{\mathrm{W}} = I_{\mathrm{rms}}^{2} \cdot \left(R_{\mathrm{dc,Litz}} \cdot F_{\mathrm{ac,Litz}} \right). \tag{56}$$

The total loss of the IMC can be determined as follows:

$$P_{\mathrm{T}} = \sum P_{\mathrm{W}} + P_{\mathrm{core}} + P_{\mathrm{shunt}} \tag{57}$$

Fig. 14 shows the loss decomposition of the proposed IMC under full-load conditions. When the output voltage is 300 V, the RMS current of the resonant-tank is high, resulting in a large proportion of winding losses. As the output voltage increases, the core loss increases, whereas the RMS current of the resonant-tank decreases, leading to reduced winding losses.

The conventional copper-bar winding of the LDC is replaced by a Litz-wire winding, by which the total winding loss can be effectively reduced. This loss consists of the ohmic loss caused by the dc resistance, the ac loss caused by the ac resistance, and the eddy-current loss induced by the external proximity effect. The corresponding expression is given as follows:

$$\begin{array}{c} \Delta P_{\mathrm{IMC}} = P_{\mathrm{IM,bar}} - P_{\mathrm{IM,Litz}} \\ = I_{\mathrm{rms}}^{2} F_{\mathrm{ac,Litz}} R_{\mathrm{dc,Litz}} \left(F_{\mathrm{ac}} - 1 \right) + P_{\mathrm{eddy\_Litz}} \left(R_{\mathrm{e}} - 1 \right) \end{array}. \tag{58}$$

V. EXPERIMENTAL RESULTS

To validate the effectiveness of the proposed IMC, a prototype, which combines a 6.6 kW SRC and a 2 kW LDC, is built. The circuit topology of the prototype is shown in Fig. 2. In conventional OBCs, Si-IGBTs are typically employed due to their reliability and low cost. However, their high switching losses restrict its efficiency and power density. In this work, 650 V SiC devices NTBG032N065M3S are adopted for the switches of the H-bridge on both sides of the SRC to achieve higher switching frequency and improved efficiency. The control algorithm is implemented on a TMS320F2800157 digital signal processor, which uses its on-chip ADC, ePWM, and CMPSS modules. The interrupt and sampling frequencies are both configured to be half of the switching frequency.

Fig. 15 shows the experimental setup. Shunt resistors are used to measure the output current of the OBC. The Chroma 62180D is used as the high-voltage power supply, while the Chroma 63204A-150-400 and EL51000A are used as the low-voltage and high-voltage electronic loads, respectively.

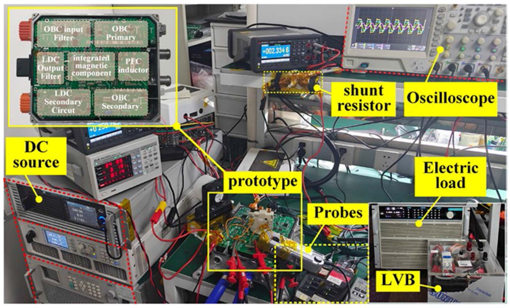

Fig. 15. Photograph of the experimental setup.

TABLE II
PARAMETERS AND DESIGN SPECIFICATIONS

Symbol	Parameters	Specifications
V_{bus}	Bus voltage	350–410 V
V_{HV}	HV output voltage	250–500 V
P_{obc}	Output power of OBC	6.6 kW
P_{LDC}	Output power of LDC	2 kW
f_s	Switching frequency	100 kHz
L_k	Leakage inductance	20.8 μH
C_r	Resonant capacitor	230 nF
N_{tran}	turns ratio	14:15:1:1
V_{LV}	LV output voltage	9–16 V

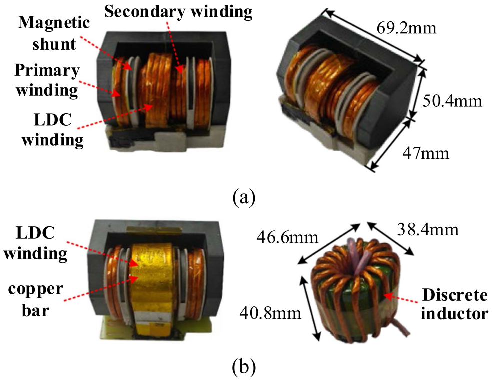

(a)

(b)

Fig. 16. Photograph of the IMC. (a) Proposed IMC. (b) Comparative magnetic component.

Table II gives the specifications of the proposed IMC. A photograph of the proposed IMC is shown in Fig. 16. The measured results of the proposed IMC are given in Table III, which are close to the these obtained from the FEA simulations. The LDC winding exhibits a low equivalent inductance, which helps minimize the voltage stress on its switching devices. In contrast, the primary winding of the SRC features a higher equivalent leakage inductance, enabling a wide ZVS range.

The measured equivalent leakage inductance of the IMC is 20.8 μH. According to the calculation of leakage inductance given in Section III, the calculated leakage inductance is 20.2 μH, which is close to the measured result, with a deviation below 5% . This deviation primarily stems from model simplifications, material properties, and assembly tolerances. Considering the measurement uncertainty, a deviation of the leakage inductance within ± 5% is acceptable.

TABLE III
PARAMETERS OF THE PROPOSED IMC

Symbol	FEA results	Measured results
L_p	17.8 μH	18.49 μH
L_s	1.73 μH	2.64 μH
L_a	19 nH	48 nH
L_b	13 nH	33 nH
L_m	1.31 mH	1.33 mH

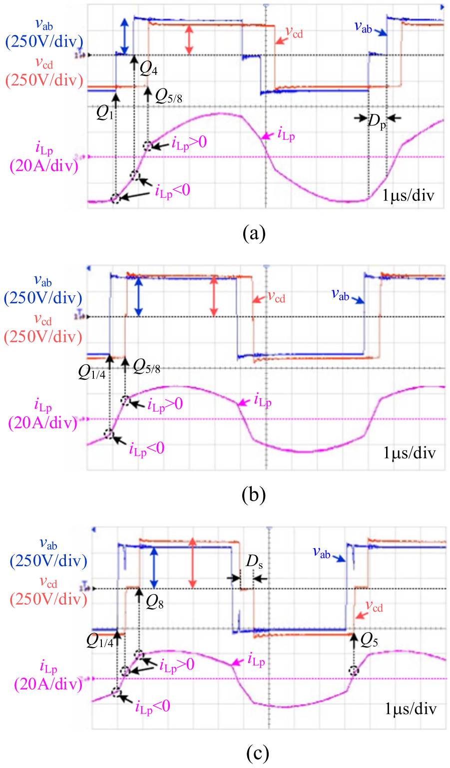

Fig. 17. Experimental waveforms under full load with different output voltage. (a) $V_{\mathrm{HV}} = 300$ V. (b) $V_{\mathrm{HV}} = 400$ V. (c) $V_{\mathrm{HV}} = 500$ V.

Fig. 17 shows the experimental waveforms with different output voltage under full-load. In Fig. 17(a), $V_{\mathrm{bus}} = 350$ V, the voltage gain is $k = nV_{\mathrm{HV}}/V_{\mathrm{bus}} = 0.8 <1$. An internal phase shift duty cycle D_p is applied between the primary-side switches Q_1 and Q_4. At the turn-ON instant of Q_1 and Q_4, the current $i_{\mathrm{Lp}} < 0$, which indicates that the output capacitances of Q_1 and Q_4 can be fully discharged, and ZVS of Q_1 and Q_4 can achieved. The rising edge of v_{cd} corresponds to the simultaneous turn-on of the secondary-side switches Q_5 and Q_8, during which $i_{\mathrm{Lp}}>0$, ZVS can also be achieved.

In Fig. 17(b), $V_{\mathrm{bus}} = 373$ V, the voltage gain is $k = 1$. The internal phase shift duty cycle D_p is reduced to zero, the OBC operates with a simple SPS modulation. It can be known that Q_1

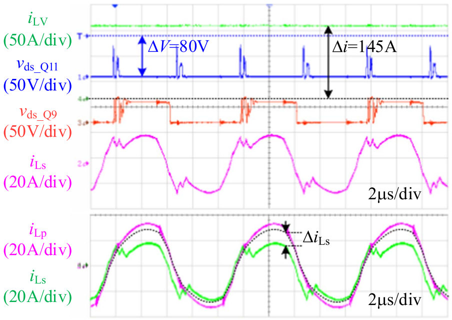

Fig. 18. Experimental results when output power of OBC is 4.6 kW and the load of LDC is 2 kW during simultaneous charging mode.

and Q_4 are turned ON simultaneously, with the corresponding resonant current $i_{\mathrm{Lp}} < 0$. Similarly, Q_5 and Q_8 are also turned ON simultaneously, and the resonant current $i_{\mathrm{Lp}} > 0$. Therefore, the SPS modulation can realize ZVS for all switches of the SRC.

In Fig. 17(c), $V_{\mathrm{bus}} = 410$ V, the voltage gain is $k = 1.14$. An internal phase shift duty cycle D_{s} is applied between the secondary-side switches Q_5 and Q_8. The resonant current $i_{\mathrm{Lp}} < 0$ at the turn-ON instant of Q_1 and Q_4, thus ZVS can be achieved. Similarly, $i_{\mathrm{Lp}} > 0$ at the turn-ON instant of Q_5 and Q_8, ZVS can be achieved as well.

It can be known from Fig. 17 that the proposed IMC can operate stably over the full voltage range of the HVB. By optimizing the modulation strategy of the SRC, wide-range ZVS operation can be achieved.

Fig. 18 shows the experimental results under simultaneous charging mode, with $V_{\mathrm{HV}} = 300$ V, $P_{\mathrm{obc}} = 4.6$ kW, and $P_{\mathrm{LDC}} = 2$ kW. It can be known that the output current of the LDC is 145 A, and the LDC draws power from the HVB, resulting in a current deviation Δi_{Ls} in the secondary winding of the SRC. The current deviation Δi_{Ls} is reflected to the LDC side based on the turns-ratio between the OBC secondary winding and the LDC winding, yielding $i_{\mathrm{Lt}} = (N_{\mathrm{s}}/N_{\mathrm{t}})\times\Delta i_{\mathrm{Ls}}$. The results show that the proposed IMC effectively supports simultaneous charging of HVB and LVB. Furthermore, small equivalent leakage inductance of LDC winding helps reduce voltage stress on the switching devices induced by high di/dt. In this work, Si devices SVGQ104R1NL5S-2HS are adopted as the switching devices of the LDC. As shown in Fig. 18, the drain–source voltage $V_{\text{ds-Q9}}$ and $V_{\text{ds-Q11}}$ remain below 80 V, providing a 20 V safety margin with respect to the rated drain-to-source breakdown voltage of 100 V.

Fig. 19 gives the measured efficiency of the proposed IMC for different HVB voltage and load conditions. It can be known that a peak efficiency of 98.17% is achieved at a load of 4200 W, validating the high-efficiency of the proposed IMC.

Fig. 20 shows the measured efficiency of the proposed IMC with Litz-wire windings, copper bar-based windings, and IMC with the discrete inductor, different HVB voltage at full-load. In the experimental prototype, the same magnetic core, winding turns and resonant inductance are used. The results show that, compared with the discrete inductor-based IMC, the proposed IMC achieves 40% reduction in volume with 0.2% decrease in average efficiency. Furthermore, compared with the copper bar-based IMC, the proposed design improves efficiency by 0.5% . These results confirm that multi-strand Litz wire effectively suppress eddy current losses induced by leakage magnetic fields, demonstrating a tradeoff between efficiency and power density in the IMC design.

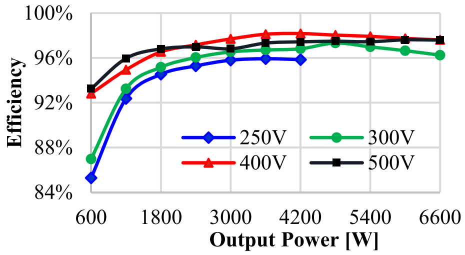

Fig. 19. Measured efficiency with different HVB voltage and load power in OBC mode.

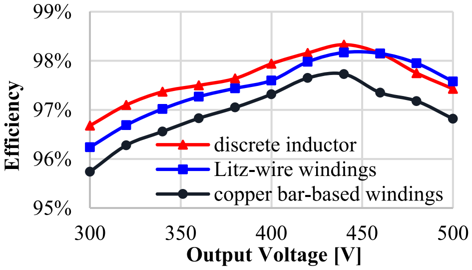

Fig. 20. Comparison of the measured efficiency of the proposed IMC with Litz-wire windings and copper bar-based windings, and the IMC with the discrete inductor, for different HVB voltages under full-load operation.

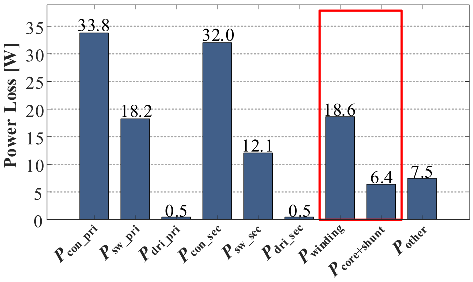

Fig. 21. Loss breakdown at the full load ($V_{\mathrm{HV}} = 420$ V).

The loss breakdown at $V_{\mathrm{HV}} = 420$ V and $P_{\mathrm{o}} = 6.6$ kW is shown in Fig. 21. $P_{\mathrm{con{\cdot}pri}}$ and $P_{\mathrm{con{\cdot}sec}}$ are the conduction losses of the primary and secondary side switches. $P_{\mathrm{sw{\cdot}pri}}$ and $P_{\mathrm{sw{\cdot}sec}}$ are the switching loss of the primary and secondary side switches. P_{winding} is the conduction loss of the proposed IMC, while $P_{\mathrm{core+shunt}}$ corresponds to the core loss of the proposed IMC including the magnetic shunts. The other losses include the ESR loss of the resonant capacitors and decoupling capacitors, and the loss in the auxiliary power supply.

To illustrate the superiority of the proposed IMC, a comparison with representative IMC-based solutions in VCS applications is presented in Tables IV and V. The HVB charging solutions of the conventional VCS are shown in Table IV, while

TABLE IV
COMPARATIVE ANALYSIS OF EXISTING HVB CHARGING SOLUTIONS

	[19]	**[18]**	**[23]**	**[32]**	**[33]**	**This work**
Output voltage	200–450 V	250–400 V	450–850 V	250–380 V	250–400 V	250–500 V
Voltage gain *k*	0.56–1.26	0.71–1.14	0.81–1	0.65–1	0.62–1	0.66–1.16
Switching frequency	>60 kHz	500–900 kHz	250 kHz	500 kHz	75–300 kHz	100 kHz
Total switches of VCS	18	18	24	18	18	16
Switch selection of OBC	650 V MOS (45 mΩ)	650 V GaN (25 mΩ)	1200 V SiC (21 mΩ)	1200 V SiC (25 mΩ)	600 V GaN (70 mΩ)	650 V SiC (32 mΩ)
Winding type	Litz wire	PCB winding	PCB winding	PCB winding	Litz wire	Litz wire
Topology	SRC	CLLC	CLLC	DAB	LLC	SRC/CTR
Output power	6.6 kW	2 kW	11 kW	3.3 kW	3.2 kW	6.6kW/2kW
Magnetic volume	13 in^3	2.57 in^3	11.5 in^3	~5.6 in^3	8.3 in^3	10 in^3
Magnetic power density	507 W/in^3	778 W/in^3	950 W/in^3	589 W/in^3	385 W/in^3	660 W/in^3
Peak efficiency	97.7%	96.8%	98.4%	98%	98.5%	98.17%

TABLE V
COMPARATIVE ANALYSIS OF EXISTING SIMULTANEOUS CHARGING SOLUTIONS

	[11]	**[7]**	**[9]**	**[13]**	**[12]**	**This work**
Output voltage of HVB	380–710 V	250–400 V	150–200 V	440–470 V	300–420 V	250–500 V
Voltage gain *k*	~1	0.62–1	0.79–1.05	0.93–1	1–1.42	0.66–1.16
Output voltage of LVB	13–16.5 V	14–16 V	12 V	40–47 V	20–28.8 V	9–16 V
Total switches of VCS	17	14	15	18	12	16
Switch selection of OBC	1200 V SiC (189 mΩ)	900 V SiC (40 mΩ)	300 V MOS (85 mΩ)	- SiC (-)	600 V MOS (17 mΩ)	650 V SiC (32 mΩ)
Switching frequency	185 kHz	88–107 kHz	70 kHz	43.76 kHz	100 kHz	100 kHz
Winding type	Litz wire	Litz wire	Litz wire	Litz wire	Litz wire	Litz wire
Topology	LLC/PSFB	LLC/PSFB	DAB/BDR	TPSRC	DAB/VDR	SRC/CTR
Output power	3.3 kW/1.8 kW	3.3 kW/1 kW	1.5 kW/0.3 kW	1.8 kW/0.5 kW	2.2 kW/0.3 kW	6.6 kW/2 kW
Magnetic volume	11.9 in^3	~24.5 in^3	14.3 in^3	> 20 in^3	~5 in^3	10 in^3
Magnetic power density	300 W/in^3	~150 W/in^3	104.5 W/in^3	< 100 W/in^3	~440 W/in^3	660 W/in^3
Peak efficiency	97.7%	97.17%	97.9%	-	95.9%	98.17%

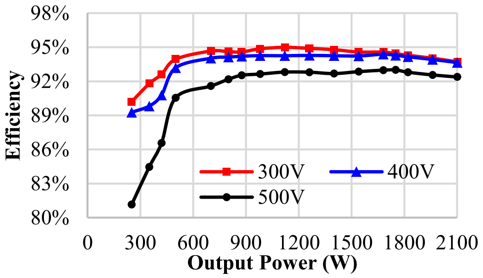

Fig. 22. Measured efficiency with different HVB voltage and load power in LDC mode ($V_{\mathrm{LV}} = 14$ V).

the simultaneous charging scheme of the integrated VCS is shown in Table V.

Fig. 22 shows the measured efficiency of the proposed IMC in LDC mode under different HVB voltages and load conditions with $V_{\mathrm{LV}} = 14$ V. The output current of the LDC is measured using a PSI400A-P high-accuracy 400-A current sensor. It can be known that the standalone operation achieves a peak efficiency of 95% at a load of 1100 W. Moreover, an efficiency greater than 90% is achieved over a wide operating range when power is delivered from HVB to LVB.

Fig. 23 shows the thermal images of the proposed IMC and the conventional IMC at $V_{\mathrm{HV}} = 300$ V and $P_{\mathrm{o}} = 6.6$ kW. All measurements were conducted under identical operating and ambient conditions, with an ambient temperature of approximately 30 °C.

The proposed IMC shows a maximum temperature of 62.6 °C, which occurs in the OBC secondary winding near the magnetic shunt. In contrast, the hottest point of the conventional IMC is on the copper-bar winding, at 111 °C. The eddy-current losses induced by the leakage flux increase the temperature of the copper-bar windings, whereas the use of Litz-wire windings

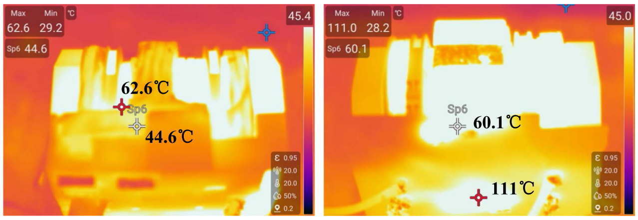

Fig. 23. Measured thermal images of the IMC ($V_{\mathrm{HV}} = 300$ V, $P_{\mathrm{o}} = 6.6$ kW). (a) Proposed. (b) Conventional.

results in a more uniform surface current distribution and lower eddy-current losses.

According to the specifications reported in the published literatures, the sizes of the magnetics were normalized to cubic inches. The power density of the magnetics is defined as the ratio of the maximum output power $P_{\mathrm{o,max}}$ of the converter to the volume V_{mag} of the integrated magnetics

$$P_{\mathrm{d,mag}} = \frac{P_{\mathrm{o,max}}}{V_{\mathrm{mag}}}. \tag{59}$$

It can be known that at high switching frequencies, planar IMC with PCB windings exhibit higher magnetic power density and improved efficiency. For instance, the CLLC resonant topology adopted in study [23] achieves a magnetic power density of 950 W/in^3 at an 800 V platform. However, to reduce conduction losses, 1200 V SiC devices with a low $R_{\mathrm{ds(on)}}$ of 21 mΩ were employed, which results in a significantly higher cost. Moreover, the parasitic capacitance between windings in planar IMCs may cause EMI, leading to severe differential-mode and common-mode noise.

For a 400 V platform, the reduced voltage at the same output power leads to increased winding current in the IMC. Consequently, as reported in [18], even with switching frequencies exceeding 500 kHz, both the magnetic power density and peak efficiency tend to decrease.

Furthermore, as a conventional VCS solution, an additional LDC, as listed in Table IV, is required for LVB charging. A typical LDC is implemented as a PSFB converter, which involves at least six additional switching devices and one isolated transformer. As a result, the overall system cost increases considerably, while the magnetic power density is substantially reduced.

At low switching frequencies, the high cost of multilayer PCB limits the adoption of planar IMCs [20]. Compared with PCB windings, Litz-wire-based IMCs exhibit a significantly lower power density. Moreover, in the integrated VCS, as shown in Table V, the power density of the IMC is further reduced. For example, in study [11], even with a switching frequency above 150 kHz, the reported magnetic power density is 300 W/in^3. Furthermore, due to the simultaneous charging operation of the integrated VCS, the high switching frequency leads to significant switching and conduction losses in the LDC, potentially causing thermal stability issues. It can be known that the IMC has become a crucial bottleneck in achieving high power density for integrated VCS.

From the comparison results, the proposed IMC in this work achieves a well tradeoff among efficiency, cost, integration, and manufacturability. The main advantages of the proposed IMC are as follows.

1) *Improved compatibility*: The proposed IMC operates over a wide HVB voltage range and requires only a simple adjustment of the turns ratio for operation on the 800 V platform, without the need for redesign or high-voltage-rated front-end components.
2) *High power density*: The proposed IMC eliminates the need for an additional isolated transformer and resonant inductor, thereby achieving a magnetic power density significantly higher than that of conventional designs.
3) *Cost-performance tradeoff*: The IMC-based system reduces the number of switching devices and efficiently handles the low-voltage, high-current output of the LDC. Its Litz-wire-based winding structure mitigates proximity losses, and by adopting cost-effective 650 V SiC devices, the system achieves high efficiency.

VI. CONCLUSION

In this article, a novel high-density IMC is proposed for vehicle charging systems, enabling the integration of three magnetic components from both the OBC and LDC stages into a single transformer structure. The proposed IMC effectively reduces the system volume and overall cost. By employing multistrand Litz wire for the LDC winding, the IMC supports low-voltage high-current output while mitigating eddy current losses induced by leakage fields. The leakage inductance of the IMC is made tunable by adjusting the geometry of the magnetic shunt. A 6.6 kW SRC and 2 kW LDC experimental prototype has been built, demonstrating a peak efficiency of 98.17% and achieving a magnetic power density of 660 W/in^3. Moreover, the proposed IMC enables simultaneous charging of both HVB and LVB, validating its effectiveness in high-performance VCS applications.

REFERENCES

[1] S. S. Williamson, A. K. Rathore, and F. Musavi, "Industrial electronics for electric transportation: Current state-of-the-art and future challenges," *IEEE Trans. Ind. Electron.*, vol. 62, no. 5, pp. 3021–3032, May 2015.

[2] A. Khaligh and M. D'Antonio, "Global trends in high-power on-board chargers for electric vehicles," *IEEE Trans. Veh. Technol.*, vol. 68, no. 4, pp. 3306–3324, Apr. 2019.

[3] L. Jiang et al., "Integrated optimization of dual-active-bridge DC–DC converter with ZVS for battery charging applications," *IEEE J. Emerg. Sel. Topics Power Electron.*, vol. 11, no. 1, pp. 288–300, Feb. 2023.

[4] Z. Fang, H. Yue, Z. Wei, Z. Zhang, and Z. Huang, "A control-free series resonant converter for battery charging with automatic CC-to-CV profile and whole-process high efficiency," *IEEE Trans. Power Electron.*, vol. 38, no. 7, pp. 8666–8675, Jul. 2023.

[5] H. Li et al., "Bidirectional control with fitting model-based synchronous rectification and input ripple current feedforward for SiC bidirectional CLLC EV charger," *IEEE Trans. Ind. Electron.*, vol. 70, no. 9, pp. 9136–9146, Sep. 2023.

[6] G. Yu and S. Choi, "An effective integration of APM and OBC with simultaneous operation and entire ZVS range for electric vehicle," *IEEE Trans. Power Electron.*, vol. 36, no. 9, pp. 10343–10354, Sep. 2021.

[7] C. -H. Jo and D. -H. Kim, "A novel integrated OBC and LDC system with improved cross-regulation performance for electric vehicles," *IEEE Trans. Ind. Electron.*, vol. 72, no. 2, pp. 1452–1465, Feb. 2025.

[8] C.-H. Jo, T.-J. Jeong, G. Li, and D.-H. Kim, “A novel integrated OBC and LDC system with flux path reconfiguration for electric vehicles,” *IEEE Trans. Power Electron.*, vol. 40, no. 1, pp. 2484–2494, Jan. 2025.

[9] I. Kim and J.-W. Park, “Integration of DC–DC converters for OBC, LDC, and TC in electric vehicles,” *IEEE Trans. Transp. Electrific.*, vol. 10, no. 3, pp. 5533–5543, Sep. 2024.

[10] I. Kim and J.-W. Park, “New integrated DC–DC conversion system for electric vehicles,” *IEEE Trans. Ind. Electron.*, vol. 71, no. 7, pp. 7126–7135, Jul. 2024.

[11] D.-W. Lee, B.-S. Lee, J.-H. Ahn, J.-Y. Kim, and J.-K. Kim, “New combined OBC and LDC system for electric vehicles with 800 V battery,” *IEEE Trans. Ind. Electron.*, vol. 69, no. 10, pp. 9938–9951, Oct. 2022.

[12] I. Kim and J.-W. Park, “Multifunctional integrated DC–DC converter for electric vehicles,” *IEEE Trans. Power Electron.*, vol. 39, no. 6, pp. 7252–7263, Jun. 2024.

[13] S. S. Chakraborty, S. Dey, and K. Hatua, “Design of a three-winding transformer for power decoupling of a three-port series resonant converter for an integrated on-board EV charger,” *IEEE Trans. Power Electron.*, vol. 38, no. 11, pp. 14262–14273, Nov. 2023.

[14] P. He, A. Mallik, A. Sankar, and A. Khaligh, “Design of a 1-MHz high-efficiency high-power-density bidirectional GaN-based CLLC converter for electric vehicles,” *IEEE Trans. Veh. Technol.*, vol. 68, no. 1, pp. 213–223, Jan. 2019.

[15] S. Arab Ansari, J. N. Davidson, and M. P. Foster, “Fully-integrated planar transformer with a segmental shunt for LLC resonant converters,” *IEEE Trans. Ind. Electron.*, vol. 69, no. 9, pp. 9145–9154, Sep. 2022.

[16] S. A. Ansari, J. N. Davidson, and M. P. Foster, “Fully-integrated transformer with asymmetric primary and secondary leakage inductances for a bidirectional resonant converter,” *IEEE Trans. Ind. Appl.*, vol. 59, no. 3, pp. 3674–3685, May/Jun. 2023.

[17] J. Yang, X. Wu, G. Liu, D. Ping, and Z. Deng, “Modeling and design of integrated inductor and transformer considering superposed flux density in on-board charger,” in *Proc. IEEE Appl. Power Electron. Conf. Expo.*, Mar. 2020, pp. 879–884.

[18] J. Yang, Y. Xu, X. Wu, and F. Muhammad, “High-density planar integrated magnetics with two-sided merged inductor windings and integrated cores for resonant DC/DC converter,” *IEEE J. Emerg. Sel. Topics Power Electron.*, vol. 12, no. 1, pp. 195–207, Feb. 2024.

[19] J. Yang, X. Wu, F. Muhammad, and Z. Deng, “External magnetic field minimization for the integrated magnetics in series resonant converter,” *IEEE Trans. Power Electron.*, vol. 37, no. 1, pp. 498–508, Jan. 2022.

[20] B. Li, Q. Li, and F. C. Lee, “High-frequency PCB winding transformer with integrated inductors for a bidirectional resonant converter,” *IEEE Trans. Power Electron.*, vol. 34, no. 7, pp. 6123–6135, Jul. 2019.

[21] S. Dey, C. Reece, O. P. Irabor, and A. Mallik, “Comparative analysis and optimization of triple active bridge transformer configuration with integrable leakage inductance,” *IEEE J. Emerg. Sel. Topics Power Electron.*, vol. 11, no. 5, pp. 5102–5119, Oct. 2023.

[22] C. Fei, F. C. Lee, and Q. Li, “High-efficiency high-power-density LLC converter with an integrated planar matrix transformer for high-output current applications,” *IEEE Trans. Ind. Electron.*, vol. 64, no. 11, pp. 9072–9082, Nov. 2017.

[23] F. Jin, A. Nabih, Z. Li, and Q. Li, “A scalable matrix integrated transformer with controllable leakage inductance for a bidirectional resonant converter,” *IEEE Trans. Power Electron.*, vol. 38, no. 9, pp. 10967–10984, Sep. 2023.

[24] Y. -S. Kim, C. -Y. Oh, W. -Y. Sung, and B. K. Lee, “Topology and control scheme of OBC–LDC integrated power unit for electric vehicles,” *IEEE Trans. Power Electron.*, vol. 32, no. 3, pp. 1731–1743, Mar. 2017.

[25] *Electric Vehicle Conductive Charging System—Part 21-2*, IEC Standard 61851-21-2, 2018.

[26] S. Lee, H. Cha, and D. -C. Lee, “Voltage balancing for triple-active-bridge converter using integrated transformer,” *IEEE J. Emerg. Sel. Topics Power Electron.*, vol. 13, no. 2, pp. 2027–2035, Apr. 2025.

[27] S. Deb and S. K. Pramanick, “Investigation of leakage inductance in three-winding transformer for three-port integrated onboard chargers,” in *Proc. IEEE Transp. Electrific. Conf. Expo.*, 2024, pp. 1–6.

[28] M. Yaqoob, K. H. Loo, and Y. M. Lai, “A four-degrees-of-freedom modulation strategy for dual-active-bridge series-resonant converter designed for total loss minimization,” *IEEE Trans. Power Electron.*, vol. 34, no. 2, pp. 1065–1081, Feb. 2019.

[29] A. Arruti, I. Aizpuru, M. Mazuela, Z. Ouyang, and M. A. E. Andersen, “Evolution of classical 1-D-based models and improved approach for the characterization of Litz wire losses,” *IEEE Trans. Power Electron.*, vol. 39, no. 12, pp. 16371–16381, Dec. 2024.

[30] E. L. Barrios, A. Ursúa, L. Marroyo, and P. Sanchis, “Analytical design methodology for Litz-wired high-frequency power transformers,” *IEEE Trans. Ind. Electron.*, vol. 62, no. 4, pp. 2103–2113, Apr. 2015.

[31] C. Peng, G. Chen, B. Wang, and J. Song, “Semi-analytical AC resistance prediction model for Litz wire winding in high-frequency transformer,” *IEEE Trans. Power Electron.*, vol. 38, no. 10, pp. 12730–12742, Oct. 2023.

[32] Y. Park, S. Chakraborty, and A. Khaligh, “DAB converter for EV onboard chargers using bare-die SiC MOSFETs and leakage-integrated planar transformer,” *IEEE Trans. Transp. Electrific.*, vol. 8, no. 1, pp. 209–224, Mar. 2022.

[33] L. A. D. Ta, N. D. Dao, and D. -C. Lee, “High-efficiency hybrid LLC resonant converter for on-board chargers of plug-in electric vehicles,” *IEEE Trans. Power Electron.*, vol. 35, no. 8, pp. 8324–8334, Aug. 2020.